Science

AAAS

Plasmonic Nanolaser Using Epitaxially Grown Silver Film
Yu-Jung Lu *et al.*
Science **337**, 450 (2012);
DOI: 10.1126/science.1223504

Plasmonic Nanolaser Using Epitaxially Grown Silver Film

Yu-Jung Lu,[1]* Jisun Kim,[2]* Hung-Ying Chen,[1] Chihhui Wu,[2] Nima Dabidian,[2] Charlotte E. Sanders,[2] Chun-Yuan Wang,[1] Ming-Yen Lu,[3] Bo-Hong Li,[4] Xianggang Qiu,[4] Wen-Hao Chang,[5] Lih-Juann Chen,[3] Gennady Shvets,[2] Chih-Kang Shih,[2]† Shangjr Gwo[1]†

A nanolaser is a key component for on-chip optical communications and computing systems. Here, we report on the low-threshold, continuous-wave operation of a subdiffraction nanolaser based on surface plasmon amplification by stimulated emission of radiation. The plasmonic nanocavity is formed between an atomically smooth epitaxial silver film and a single optically pumped nanorod consisting of an epitaxial gallium nitride shell and an indium gallium nitride core acting as gain medium. The atomic smoothness of the metallic film is crucial for reducing the modal volume and plasmonic losses. Bimodal lasing with similar pumping thresholds was experimentally observed, and polarization properties of the two modes were used to unambiguously identify them with theoretically predicted modes. The all-epitaxial approach opens a scalable platform for low-loss, active nanoplasmonics.

Miniaturization of semiconductor lasers holds the key to emerging applications in on-chip integration of nanophotonics and nanoelectronics (*1–3*). Currently, miniaturization of semiconductor lasers based on dielectric optical cavities is impeded by the diffraction limit—that is, $\sim(\lambda/2n)^3$ for three-dimensional (3D) cavities, where λ is the free-space wavelength and n is the refractive index of the dielectric (*4–7*). The recent advent of nanoplasmonics based on metallodielectric structures has led to the design of optical components and optoelectronic devices in the deep subwavelength regime (*8–13*). In particular, a new class of lasers based on surface plasmon amplification by stimulated emission of radiation (SPASER) has been proposed (*14, 15*) and experimentally demonstrated (*16–19*). Surface plasmon polaritons (SPPs) excited in noble metal structures adjacent to gain media dramatically shrink the optical mode volume and provide the necessary feedback mechanism for a SPASER.

Among the available plasmonic cavity materials in the visible and near-infrared ranges, silver (Ag) is the best choice because of its minimal plasmonic damping (*20*). However, so far most plasmonic devices have their basis in granular polycrystalline Ag films, where surface roughness and grain boundaries lead to scattering of SPPs. Thus, atomically smooth or single-crystalline plasmonic structures are desirable building blocks for low-loss applications (*21, 22*).

With use of polycrystalline metallic materials, the lasing threshold for plasmonic nanolasers remains impractically high, and the continuous-wave (CW) operation of a plasmonic laser has yet to be demonstrated (*16–19*).

Having developed epitaxially grown, atomically smooth Ag films as a scalable plasmonic platform, we report a SPASER under CW operation with an ultralow lasing threshold at liquid nitrogen temperature and a mode volume well below the 3D diffraction limit. The device has its basis in the plasmonic nanocavity formed between epitaxial Ag film and a single nanorod consisting of a gallium nitride (GaN) shell and a green-emitting indium gallium nitride (InGaN) core, which acts as gain medium and which was

chosen, in part, for its relatively large optical gain (*23*).

Under normal growth conditions, the non-wetting nature of low-loss noble metals on semiconductor or insulator substrates leads to granular film growth. The key to achieving smooth single-crystalline Ag film is to refine a two-step process (low-temperature deposition followed by room-temperature annealing) originally developed for GaAs(110) substrates (*24, 25*) and to apply it to the silicon surface [Si(111), 7×7 reconstruction] (*26*). However, dewetting eventually occurs (*25*). This problem is solved by capping the as-grown Ag film with a thin dielectric layer.

During deposition at low temperature (90 K), Ag forms nanoclusters, as indicated by a spotty reflection high-energy electron diffraction (RHEED) pattern Fig. 1A, top). Upon annealing to room temperature, these nanoclusters smoothen, as indicated by streaky RHEED patterns (Fig. 1A, bottom). In situ scanning tunneling microscopy (STM) reveals that the surface is atomically smooth (Fig. 1B), with a surface step structure similar to that of the underlying Si(111) surface. The large-area film uniformity is confirmed by scanning tunneling spectroscopy (STS) (Fig. 1C), which reveals identical quantum well states at different locations on the sample surface (*24, 25*). At the end of growth, the sample is capped with about 1.5 nm of amorphous germanium (Ge) grown by molecular beam epitaxy (MBE). Atomic force microscopy (AFM) reveals that the Ge-capped Ag film remains atomically smooth in air (Fig. 1D).

The nanocavity is defined by a GaN nanorod (480 nm in length) partially filled with an InGaN gain medium (170 nm in length) and separated
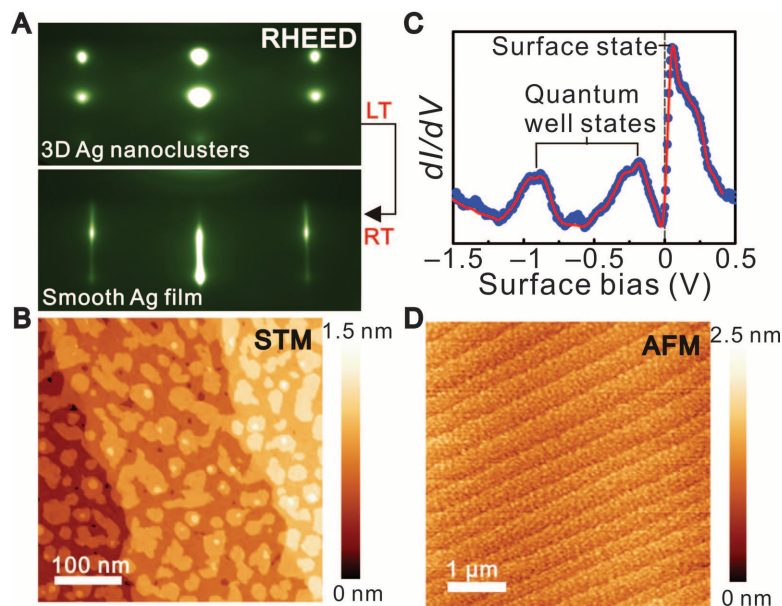
[1]Department of Physics, National Tsing-Hua University, Hsinchu 30013, Taiwan. [2]Department of Physics, The University of Texas at Austin, Austin, Texas 78712, USA. [3]Department of Materials Science and Engineering, National Tsing-Hua University, Hsinchu 30013, Taiwan. [4]Beijing National Laboratory for Condensed Matter Physics and Institute of Physics, Chinese Academy of Sciences, Beijing 100190, China. [5]Department of Electrophysics, National Chiao-Tung University, Hsinchu 30010, Taiwan.

*These authors contributed equally to this work.
†To whom correspondence should be addressed. E-mail: shih@physics.utexas.edu (C.-K.S.); gwo@phys.nthu.edu.tw (S.G.)

Fig. 1. (A) RHEED patterns taken during the two-step growth process. At low temperature (LT, 90 K), 3D Ag nanoclusters are observed after Ag deposition on Si(111). After room-temperature (RT) annealing, atomically smooth epitaxial Ag film forms. **(B)** In situ STM image of an atomically smooth epitaxial Ag film (4-nm thickness). **(C)** STS spectrum showing multiple quantum-well states and a surface state on epitaxial Ag film. Raw data (blue line) are shown with a superimposed smoothed spectrum (red line). **(D)** AFM image showing that Ge-capped Ag film remains atomically smooth in air (at RT).

by a 5-nm silicon dioxide (SiO_2) spacer from the epitaxial Ag (Fig. 2A). A nanoscale metal-oxide-semiconductor (MOS) structure is adopted here to confine the electromagnetic field in the low-dielectric-constant oxide nanogap, which greatly reduces plasmonic loss (27). The InGaN@GaN core-shell nanorods were grown on Si(111) by plasma-assisted MBE (26), with the nanorods growing along the wurtzite polar c-axis direction (28). Detailed structural information about the InGaN@GaN core-shell nanorods is given in Fig. 2, B and C.

Because the Ag layer is atomically flat and the core-shell nanorod has well-defined facets and contact geometry, a low-loss plasmonic cavity with atomically smooth interfaces is formed between them. Strong plasmonic confinement enables extraordinary localization of the hybrid optical mode around the nanorod, resulting in excellent spatial overlap between the mode and the gain medium and enabling the ultralow-threshold CW lasing operation in a diffraction-unlimited footprint. Figure 3A shows CW lasing spectra from a single nanorod at 78 K under varying optical power densities excited by a CW semiconductor diode laser at 405 nm. The scanning electron microscope (SEM) image in Fig. 2B depicts the actual core-shell nanorod on the epi-

taxial Ag film that was used for the reported lasing measurements. Two lasing peaks can be observed, at 510 and 522 nm. Investigations carried out with similar InGaN@GaN core-shell nanorods on a 20-nm polycrystalline Ag film (26) covered with a 5-nm SiO_2 spacer layer confirm that no lasing phenomena can be observed even at 8 K [under either continuous or pulsed pumping conditions; see figs. S6 and S7 (26)], which indicates the critical role of atomically smooth epitaxial Ag film for the observation of plasmonic lasing.

A light-light (L-L) plot shows the output power of the lasing mode at 510 nm as a function of pump power for two different temperatures, 8 and 78 K (Fig. 3B). The lasing signature can be seen from the concurrent onset of the linewidth narrowing plateau and the nonlinear kink of the "S"-shaped L-L plot. The lasing thresholds are 2.1 and 3.7 kW/cm^2 for the temperatures 8 and 78 K, respectively. For a single nanorod, these power densities correspond to threshold powers of 56 and 100 nW at the respective temperatures. In comparison with previously reported lasing thresholds for MOS-based plasmonic nanolasers under pulsed mode, our CW thresholds are at least two orders of magnitude smaller (17–19). Moreover, a high spontaneous-emission

coupling factor β is estimated at 0.73, on the basis of fitting the L-L plot at 8 K; this indicates that the plasmonic cavity can effectively restrict undesired spontaneous emission in a single plasmonic mode under lasing conditions. The temperature-dependent emission properties, with lasing occurring for temperatures below 120 K (Fig. 3C), show that at higher temperatures only spontaneous emission occurs; this is because the reduced gain in InGaN cannot overcome the losses for the present device structure. The weak emissions at 532 and 556 nm, according to their L-L plots, are nonlasing peaks. The availability of multiple modes (510 and 522 nm) for such an ultrasmall cavity is due to the strong wavelength compression effects in plasmonic cavities. The second-order photon correlation function, $g^{(2)}(\tau)$, can provide another unambiguous signature for lasing in small cavities (7). As shown in Fig. 3D, below the lasing threshold $g^{(2)}(\tau = 0)$ is greater than one, signifying spontaneous emission. Above the lasing threshold, we confirm that $g^{(2)}(0) = 1$ and remains at unity for all τ, which is an unambiguous signature for the temporal coherence of lasing.

Three-dimensional simulations of the plasmonic nanolaser using COMSOL finite-element code (www.comsol.com) were carried out to clarify the nature of the two lasing modes, to determine their quality factors (Q factors) and lasing thresholds, and to elucidate the role of the atomically smooth Ag film in low-pumping-threshold lasing. The optical response of InGaN was described by an idealized single-resonance frequency-dependent permittivity function $\varepsilon_g = \varepsilon_\infty^g - \frac{\omega_p^2}{\omega_G^2 - \omega^2 - i2\omega\gamma_G}$.

Here, ω_G is the emission peak; ε_∞^g is the high-frequency permittivity of the gain medium; $\gamma_G = \omega_G/2Q_{nr}$ is the nonradiative linewidth of the emitters, with Q_{nr} the emitters' nonradiative Q factor ($Q_{nr} \approx 17$); and ω_p is the effective plasma frequency of photoexcited carriers, as determined by the population inversion and proportional to the pumping power. The eigenvalue simulations reveal the existence of two dominant high-Q modes [labeled $Q^{(n)}$, where n is the integer number of charge density nodes inside the semiconductor rod] spectrally overlapping with the gain region responsible for lowest-threshold lasing. In the absence of optical pumping (i.e., for $\omega_p^2 = 0$), these n = 5 and n = 4 modes have the highest Q factors—$Q^{(5)} \approx 13$ and $Q^{(4)} \approx 9$—and Purcell factors—$F_P^{(5)} \approx 1.8$ and $F_P^{(4)} \approx 1.4$, respectively—as well as strongly subdiffraction mode volumes, $V \approx 0.03\lambda^3$ (26). The free-space emission profiles for the two modes are very different and can be easily identified. The n = 5 mode possesses a finite electric dipole moment d_x along the rod's length, responsible for highly x-polarized far-field emission, as shown in Fig. 4A (a schematic of the emission geometry is shown in Fig. 4C). On the contrary, $d_x = 0$ for the n = 4 mode, and the far-field radiation is dominated by the nonvanishing quadrupolar moments Q_{xx} and Q_{yy} (29) of the total charge distribution inside the hybrid plasmonic/photonic antenna. The emitted light's
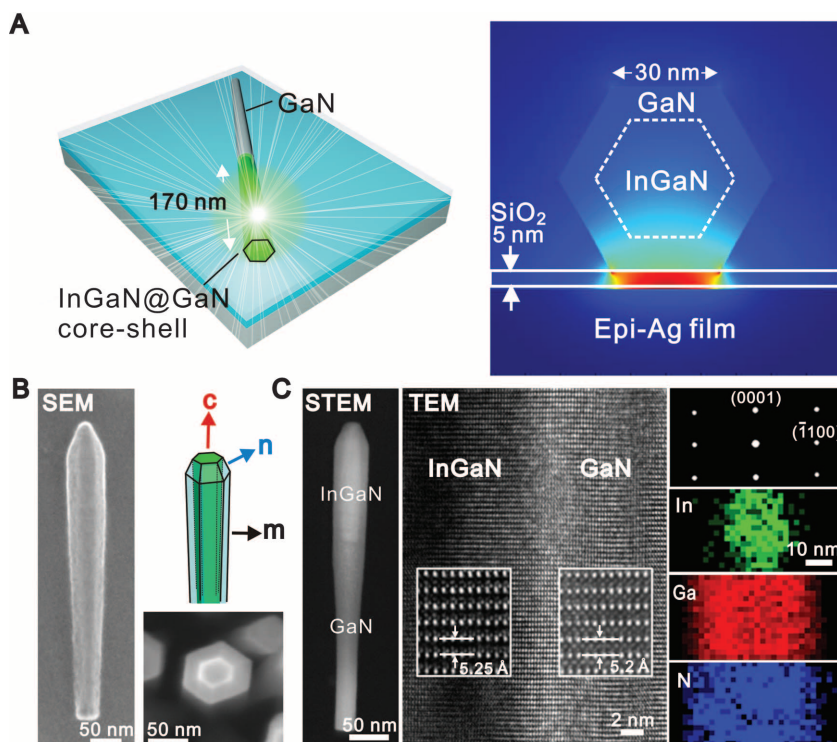

Fig. 2. (**A**) Schematic of device: a single InGaN@GaN core-shell nanorod on a SiO_2-covered epitaxial Ag film (28 nm thick). The energy-density distribution (right) is calculated by the eigenmode method. (**B**) SEM images of InGaN@GaN core-shell nanorods. The left-hand SEM image shows the actual nanorod on epitaxial Ag film that was used for all lasing measurements. (**C**) Scanning transmission electron microscopy (STEM) and transmission electron microscopy (TEM) structural analyses of a single-crystalline InGaN@GaN core-shell nanorod. The bright area inside the nanorod in the high-angle angular dark field STEM image indicates the presence of the InGaN core. The elemental mapping images obtained by energy dispersive x-ray spectroscopy are used to confirm the core-shell structure and to estimate the In composition in InGaN core (~14%).
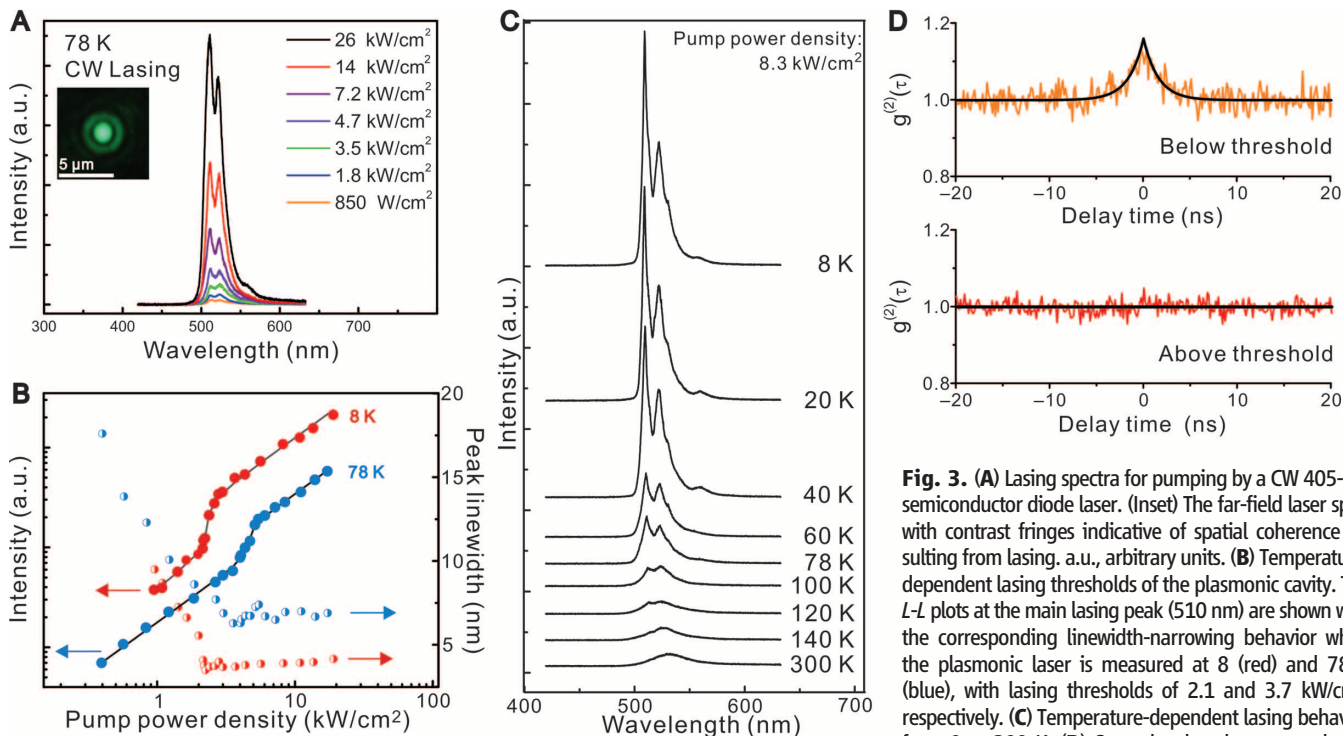
Fig. 3. (**A**) Lasing spectra for pumping by a CW 405-nm semiconductor diode laser. (Inset) The far-field laser spot, with contrast fringes indicative of spatial coherence resulting from lasing. a.u., arbitrary units. (**B**) Temperature-dependent lasing thresholds of the plasmonic cavity. The *L-L* plots at the main lasing peak (510 nm) are shown with the corresponding linewidth-narrowing behavior when the plasmonic laser is measured at 8 (red) and 78 K (blue), with lasing thresholds of 2.1 and 3.7 kW/cm^2, respectively. (**C**) Temperature-dependent lasing behavior from 8 to 300 K. (**D**) Second-order photon correlation function measurements at 8 K.

polarization is mixed between *x* and *y* (Fig. 4B). Indeed, as can be seen from Fig. 4D, the experimentally observed bimodal lasing modes (510 and 522 nm) are highly polarized along the rod axis, with a polarization ratio of 96% for the 510-nm mode and 60% for the 522-nm mode (simulation predicts 100% and 69% polarization, respectively, for a collection geometry with a numerical aperture = 0.55 objective).

Eigenvalue simulations (*26*) clarify the relative importance of the four physical processes determining the modes' lifetimes: ohmic loss in the metal, emission of SPPs to outside the cavity, radiation leakage into the substrate, and far-field emission. The most important lifetime-limiting factor is SPP emission to outside the cavity; this, for atomically smooth metal, occurs only at the ends of the GaN nanorod. Therefore, the nanolaser is a highly efficient source of coherent SPPs and can be classified as a SPASER (Fig. 4C). The prevalence of SPP generation also explains why atomically smooth metal is crucial for low-threshold CW lasing: Grain boundaries in polycrystalline Ag cause additional SPPs to be scattered out of the cavity. Our 3D simulations indicate a precipitous increase in modal volume for granular Ag (*26*), which explains the absence of CW lasing for polycrystalline Ag in the present experiment. Simulations also show that, because modes' intrinsic *Q* factors are comparable with the nonradiative *Q* factors of the emitters [$Q_{nr} \approx Q^{(n)}$], considerable hybridization between inhomogeneously broadened emitters and plasmonic modes takes place as ω_p^2 increases with pumping. Considerable blue-shifting (*26*) and rapid linewidth

decrease of the emitter and nanocavity polaritons are the main experimentally observed signatures of such hybridization.

In summary, the development of atomically smooth epitaxial Ag on Si as a new platform

for plasmonics not only allows us to demonstrate a SPASER-enabled nanolaser but also promotes the development of monolithically integrated plasmonics and Si-based electronics on a single platform.
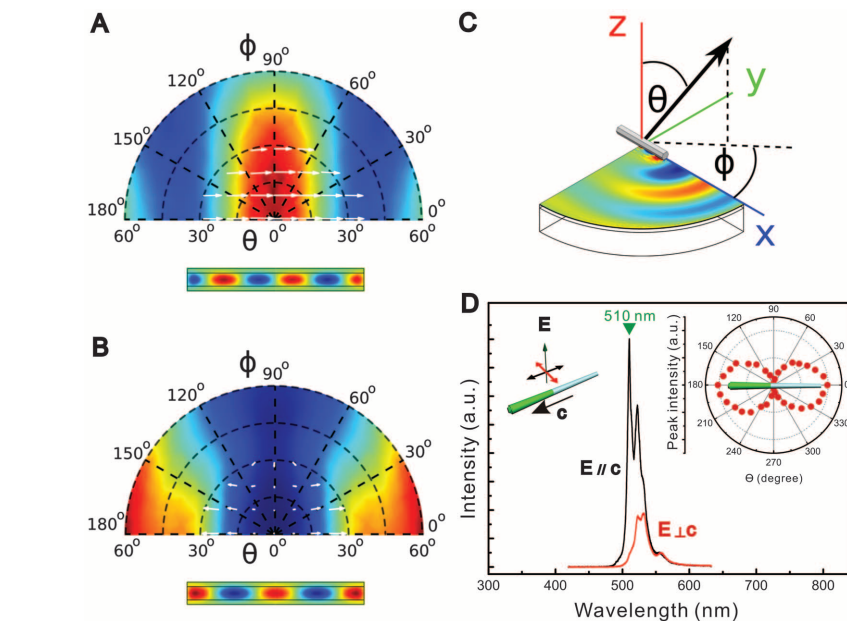

Fig. 4. (**A** and **B**) Simulations of the far-field radiation patterns (color-coded far-field radiation intensity) for two experimentally observed lasing modes. Surface charge distribution below the nanorod is color-coded. (**C**) Simulated emission geometry, showing that in-plane coherent SPPs are generated at the ends of the GaN nanorod. (**D**) Polarization-sensitive lasing spectra at 8 K, with the emission polarization oriented parallel (black curve) and perpendicular (red curve) to the nanorod axis (the *c* axis of wurtzite structure). (Inset) The polar plot of the emission intensity at 510 nm.

References and Notes

1. S. Noda, *Science* **314**, 260 (2006).
2. H. Altug, D. Englund, J. Vučković, *Nat. Phys.* **2**, 484 (2006).
3. M. T. Hill, *J. Opt. Soc. Am. B* **27**, B36 (2010).
4. K. J. Vahala, *Nature* **424**, 839 (2003).
5. O. Painter *et al.*, *Science* **284**, 1819 (1999).
6. A. Tandaechanurat *et al.*, *Nat. Photonics* **5**, 91 (2011).
7. S. Strauf, F. Jahnke, *Laser Photon. Rev.* **5**, 607 (2011).
8. W. L. Barnes, A. Dereux, T. W. Ebbesen, *Nature* **424**, 824 (2003).
9. S. A. Maier, H. A. Atwater, *J. Appl. Phys.* **98**, 011101 (2005).
10. D. K. Gramotnev, S. I. Bozhevolnyi, *Nat. Photonics* **4**, 83 (2010).
11. J. A. Schuller *et al.*, *Nat. Mater.* **9**, 193 (2010).
12. M. T. Hill *et al.*, *Nat. Photonics* **1**, 589 (2007).
13. M. P. Nezhad *et al.*, *Nat. Photonics* **4**, 395 (2010).
14. D. J. Bergman, M. I. Stockman, *Phys. Rev. Lett.* **90**, 027402 (2003).
15. M. I. Stockman, *J. Opt.* **12**, 024004 (2010).
16. M. A. Noginov *et al.*, *Nature* **460**, 1110 (2009).
17. R. F. Oulton *et al.*, *Nature* **461**, 629 (2009).
18. R.-M. Ma, R. F. Oulton, V. J. Sorger, G. Bartal, X. Zhang, *Nat. Mater.* **10**, 110 (2011).
19. C.-Y. Wu *et al.*, *Nano Lett.* **11**, 4256 (2011).
20. P. R. West *et al.*, *Laser Photon. Rev.* **4**, 795 (2010).
21. P. Nagpal, N. C. Lindquist, S.-H. Oh, D. J. Norris, *Science* **325**, 594 (2009).
22. J.-S. Huang *et al.*, *Nat. Commun.* **1**, 150 (2010).
23. K. L. Shaklee, R. E. Nahory, R. F. Leheny, *J. Lumin.* **7**, 284 (1973).
24. A. R. Smith, K.-J. Chao, Q. Niu, C. K. Shih, *Science* **273**, 226 (1996).
25. H. Yu *et al.*, *Phys. Rev. Lett.* **88**, 016102 (2001).
26. Information on methods, analyses, and simulations can be found in the supplementary materials available on *Science* Online.
27. R. F. Oulton, V. J. Sorger, D. A. Genov, D. F. P. Pile, X. Zhang, *Nat. Photonics* **2**, 496 (2008).
28. Y.-J. Lu, H.-W. Lin, H.-Y. Chen, Y.-C. Yang, S. Gwo, *Appl. Phys. Lett.* **98**, 233101 (2011).
29. J. D. Jackson, *Classical Electrodynamics* (Wiley, New York, ed. 3, 1999), chap. 9.

Supplementary Materials

www.sciencemag.org/cgi/content/full/337/6093/450/DC1
Materials and Methods
Supplementary Text
Figs. S1 to S7
References (*30–34*)

Supplementary Materials for

Plasmonic Nanolaser Using Epitaxially Grown Silver Film

Yu-Jung Lu, Jisun Kim, Hung-Ying Chen, Chihhui Wu, Nima Dabidian, Charlotte E. Sanders, Chun-Yuan Wang, Ming-Yen Lu, Bo-Hong Li, Xianggang Qiu, Wen-Hao Chang, Lih-Juann Chen, Gennady Shvets, Chih-Kang Shih,* Shangjr Gwo*

*To whom correspondence should be addressed. E-mail: shih@physics.utexas.edu (C.-K.S.); gwo@phys.nthu.edu.tw (S.G.)

This PDF file includes:

Materials and Methods
Supplementary Text
Figs. S1 to S7
References

Materials and Methods

Silver Epitaxial Film

Atomically smooth epitaxial silver (Ag) films are prepared using a refined two-step growth process (*24*): low temperature deposition of Ag followed by annealing at room temperature. First, a 2.5-nm-thick Ag film is deposited onto a silicon substrate (Si(111), flashed to 7x7 surface reconstruction) at 90 K with a low deposition rate of ~1 Å per min. It is then annealed to room temperature for about one hour. If one keeps this very thin film at room temperature, it de-wets in as little as 24 hours. However, on such an initial film, and before the de-wetting process begins, subsequent deposition is carried out using a two-step growth process similar to the one already described: deposition of film at 90 K, and annealing at room temperature for about 3 hours. We have used this procedure to grow film up to a thickness of 80 nm. For thinner films, in order to prevent de-wetting an amorphous germanium (Ge) capping layer with a thickness of ~1 nm is deposited. This capping procedure stabilizes and passivates the epitaxial Ag film. In a separate deposition system, a 5-nm-thick silicon dioxide (SiO_2) dielectric layer is deposited on top of the Ge capping layer using an ultra-high vacuum (UHV) electron-beam evaporator.

InGaN@GaN Core-Shell Nanorod

The catalyst-free, vertically-aligned InGaN@GaN core-shell nanorod array used in this study was grown on a 3-inch Si(111) wafer by plasma-assisted molecular-beam epitaxy (PA-MBE). For our growth method it is necessary to grow a GaN nanorod array as the initial growth template for subsequent growth of InGaN@GaN core-shell nanorods with regular crystalline facets. This is because the growth of InGaN nanorods without the GaN nanorod template leads to coalesced InGaN nanorods and irregular cross sectional shapes.

Following the method used in our previous study (*30*), the length of the GaN nanorods was chosen so as to prevent the onset of nanorod coalescence. In consequence, the filling factor of the InGaN gain medium in our nanolaser structure is only about 1/3. Thus, the large optical gain of InGaN plays a critical role in the realization of lasing. According to Shaklee *et al.* (*23*), GaN has a large gain coefficient of ~10,000 cm^{-1}. We anticipate that InGaN (In composition: 14%) should have a similar gain coefficient (*31*). This coefficient is about a factor of 50 larger than that of the CdS gain medium used in previous studies (*17*, *32*). Because of the large gain coefficient of InGaN, even with our low filling factor we have already achieved continuous-wave (CW) operation with low threshold at operation temperatures up to 120 K. By optimizing the growth conditions in future studies, we should be able to increase the filling factor of the InGaN@GaN core-shell nanorods so as to achieve higher operation temperatures.

After PA-MBE growth, the sample was dipped in 1% hydrogen fluoride (HF) solution for 30 sec, in order to remove the native oxide covering on the nanorods. The sample was then suspended in an isopropanol solution using a sonic bath, and individual InGaN@GaN nanorods were dispersed onto the epitaxial Ag film (already capped with 1.5 nm Ge and a 5-nm-thick SiO_2 layer). As control experiments, we performed photoluminescence measurements for single InGaN@GaN core-shell nanorods on a quartz substrate and on a polycrystalline Ag film at 8 K

(see Figs. S5 and S6); we confirmed that no lasing mode could be observed.

The crystal structure and composition of the InGaN@GaN nanorods were characterized by Cs-corrected scanning transmission electron microscope (STEM, JEOL ARM200F) at 200 kV operation voltage. This microscope is equipped with a spherical aberration corrector (CEOS GmbH) and analytical capability for energy dispersive X-ray spectroscopy (EDS).

Growth of Polycrystalline Ag Film for the Control Experiments (Figs. S6 and S7)

The polycrystalline Ag film was deposited using a UHV electron-beam evaporator. The film thickness of the polycrystalline Ag film was ~20 nm, and the film was deposited on a quartz substrate. Within the limit of scanning electron microscope (SEM) resolution (<5 nm), the films grown using this method were confirmed to be continuous.

Optical Measurements of Lasing Characteristics

We used a CW semiconductor laser diode at 405 nm as the optical excitation light source. The optical excitation and collection of emission from a single nanorod were carried out using the same 100× objective lens (Mitutoyo, N.A. = 0.55) in normal incidence/collection geometry, and the emission was dispersed by a spectrometer (HR460, Jobin-Yvon) equipped with a liquid-nitrogen-cooled charge-coupled device. The sample was mounted in a liquid-helium-flow cryostat with tunable temperatures from 8 K to 300 K.

Second Order Photon Correlation Function Measurement

The optical emission from the main plasmonic cavity mode was collected by a Hanbury Brown and Twiss (HBT) interferometer with a 50/50 beam splitter. The second order photon correlation function $g^{(2)}(\tau)$ signal was detected by a pair of Si avalanche photodiodes and time-correlated photon counting electronics.

Supplementary Text: Theoretical Modeling of the SPASER

Two-Dimensional Modeling of Hybrid SPPs

The key to low-threshold lasing is high spatial confinement of the electromagnetic modes which originate from the hybridization between a semiconductor nanorod and the surface plasmon polaritons (SPPs) supported by the Ag film. Because of the finite length $L = 480$ nm of the nanorod, a discrete set of such plasmonic cavity modes is defined by the Fabry-Perot resonance condition on the propagation wavenumber of the hybrid SPPs along the rod: $\beta^{(n)} = n\pi / L$, where n is an integer number denoting the number of nodes of charge density along the rod. We used the finite element method (FEM) based solver COMSOL to calculate the dispersion relation $\beta(\omega)$ (with $\omega = 2\pi c / \lambda$) of the hybrid SPPs and identify the discrete modes with the highest Purcell factor which overlap the inhomogeneously broadened spontaneous emission spectrum. A typical two-dimensional (2D) simulation domain is shown in the inset of

Fig. S1B: a uniform hexagonal rod with a width of 65 nm is separated from a 28-nm-thick silver film by 1 nm thick Ge and 5 nm thick SiO$_2$ layers. The Ag film rests on a Si substrate. The refractive indices of the semiconductor (GaN) nanorod, SiO$_2$, and Ge spacers are assumed to be $n_s = 2.5$, $n_{SiO_2} = 1.47$, and $n_{Ge} = 4.5 + 0.2i$, respectively. The optical dielectric permittivity of Ag is assumed to be described by the Drude model according to $\varepsilon_{Ag} = \varepsilon_\infty^{Ag} - \dfrac{\omega_p^2}{\omega(\omega + i\omega_c)}$, where

$\varepsilon_\infty^{Ag} = 3.8$ is the high frequency permittivity, $\omega_p = 1.26 \times 10^{16}$ rad/s is the plasma frequency, and $\omega_c = 6.7 \times 10^{13}$ rad/s is the collision frequency. For each frequency ω the complex propagation constant β along the rod was calculated as an eigenvalue. The calculated dispersion relation $\beta(\omega)$ is shown in Fig. S1A, and the field profile of the SPP mode is shown in the inset of Fig. S1B. The 2D Purcell factor associated with the hybrid SPP is given by

$$F_P = \frac{3}{4\pi} \frac{c}{v_g} \frac{\lambda^2}{n_g^3 A_{\text{mode}}}, \qquad \text{(S1)}$$

where v_g is the mode's group velocity and n_g is the local refractive index. A_{mode} is the effective modal area defined by $A_{\text{mode}} = 2 A_g U / (\varepsilon_g \int_G d^2 x \,|E|^2)$, where integration is over the gain medium, A_g is the area occupied by the gain medium, E is the electric field of the resonant mode, and $\varepsilon_g \approx n_g^2$ is the permittivity of the gain medium. $U = \frac{1}{4} \int d^3 x (\frac{d(\omega\varepsilon)}{d\omega} |E|^2 + \mu |H|^2)$ is the total modal energy per unit length, where E and H are the electric and magnetic fields of the resonant mode, and the integral is taken over all space, with ε and μ the local permittivity and permeability at each point. The Purcell factor plotted in Fig. S1B reaches its maximum close to $\lambda = 490$ nm, where the group velocity is greatly reduced ($\sim c/20$) and the modal area is small (about twice the area of the rod).

The modes corresponding to $n = 4$ (quadrupole mode with $\lambda_Q = 507$ nm) and $n = 5$ (dipole mode with $\lambda_D = 492$ nm) are of interest because their Purcell factors are enhanced and their resonant wavelengths fall within the bandwidth of the emitter. The Purcell factor obtained from 2D simulations is an upper limit: it does not take into account the reduction of the Q-factor due to the emission of SPPs from the tips of the nanorod. As discussed below, three-dimensional (3D) simulations yield substantially lower Purcell factors.

Three-Dimensional Simulations and the Calculation of Purcell Factors

We have performed first-principles FEM simulations of the 3D system comprised of a finite-sized active InGaN@GaN nanorod separated by a SiO$_2$/Ge spacer from a finite-thickness Ag film. The composition of the simulation domain is shown in Fig. 4C of the main text. All geometrical and physical parameters (including the finite length $L = 480$ nm of the nanorod) are

the same as in the 2D simulations described above. The calculated resonant plasmonic modes are shown in Fig. 4 of the main text.

To calculate the Purcell factor of the plasmonic modes, we solved for the 3D eigenmodes of the system. The Q-factors are calculated from the eigenmodes according to $Q = \omega U / S$, where U is the energy of the eigenmode and S is the rate of energy loss including Ohmic loss, far-field radiation into vacuum, SPP emission along the Ag surface, and radiation leakage into the Si substrate. The Purcell factor can then be evaluated according to

$$F_P = \frac{3}{4\pi^2}(\frac{\lambda}{n_g})^3(\frac{Q}{V_{mode}}), \qquad (S2)$$

where the mode volume, V_{mode}, is defined as

$$V_{mode} = \frac{2V_{rod}U}{\int_G d^3x\varepsilon_g \mid E \mid^2}; \qquad (S3)$$

integration is over the gain medium, and V_{rod} is the volume of the gain medium.

The eigenmode possessing a finite dipole moment d_x along the nanorod is calculated to be close to λ_D = 492 nm. This Fabry-Perot resonance approximately corresponds to the $n = 5$ mode found from 2D simulations. It has a Q-factor $Q^{(5)} \approx 12.6$ and a mode volume $V_D \approx 4\times10^{-21}$ m^3 $\approx 3.3\times10^{-2}\lambda^3$ (about 3 times the volume of the rod), yielding the Purcell factor $F_P^{(5)} \approx 1.84$. The breakdown of various energy losses associated with the dipolar mode is as follows: 26% is due to Ohmic loss inside the metal and the Ge layer, 28% is emitted into SPPs along the Ag surface, 32% leaks into the substrate, and 14% is emitted as far-field radiation into vacuum. The far-field radiation is the only experimentally measured quantity. Because of the finite dipole moment of the mode, this radiation is purely x-polarized, as indeed observed in the experiment.

The eigenmode possessing a vanishing dipole moment and finite quadrupole moment is calculated to be close to λ_Q = 507 nm. This Fabry-Perot resonance approximately corresponds to the $n = 4$ mode found from 2D simulations. It has a Q-factor $Q^{(4)} \approx 8.9$ and a mode volume $V_Q \approx 3.9\times10^{-21}$ m^3 $\approx 3\times10^{-2}\lambda^3$, yielding the Purcell factor $F_P^{(4)} \approx 1.44$. The loss breakdown for the quadrupolar mode is as follows: 14% of the loss is Ohmic, 37% is emitted into SPPs, 35% leaks into the substrate, and 14% is emitted into vacuum. According to the simulation, the far-field emission collected by a lens with numerical aperture N.A. = 0.55 has mixed polarization: about 84.5% x-polarized and 15.5% y-polarized light, corresponding to a polarization ratio of 69%, in good agreement with the experiment.

To demonstrate the effect of gain on the spectrum of emitted radiation (i.e., spectral narrowing with increasing gain) we have also performed current-driven simulations using

COMSOL. The simulation domain setup is identical to that of the eigenmode calculations, except that a point dipole was inserted near the tip of the rod in order to drive the system. The permittivity of the gain medium is described with a two-level transition model ,

$$\varepsilon_g = \varepsilon_\infty^g - \frac{\omega_p{}^2}{\omega_G{}^2 - \omega^2 - i2\omega\gamma_G}, \qquad (S4)$$

where ε_∞^g is the high frequency permittivity of the gain medium. The emission band is centered at $\lambda_G \equiv 2\pi c / \omega_G = 510$ nm, with full width at half maximum (FWHM) $2\lambda_G\gamma_G / \omega_G = 30$ nm, and γ_G the non-radiative linewidth of the emitter. Figure S2 shows the spectra collected in the far-field as the gain coefficient increases from $\omega_p = 5.8 \times 10^{14}$ rad/s to $\omega_p = 8.7 \times 10^{14}$ rad/s (corresponding to the density of photoexcited carriers increasing from $n_c = 1.8 \times 10^{19} / \text{cm}^3$ to $n_c = 4 \times 10^{19} / \text{cm}^3$) using the definition of the plasma frequency $\omega_p{}^2 = n_c e^2 / \varepsilon_0 m^*$, with n_c the density of photoexcited carriers and $m^* \approx 0.17 m_0$ the effective mass of the carrier electrons.

Semi-analytic Theory of Coupling Between the Plasmonic Cavity and Inhomogeneously Broadened Emitters: The Coupled-Modes Approach

Despite the small mode volumes associated with the subwavelength plasmonic cavity modes, the Q-factors are limited by material loss, far-field leakage, and SPP emission. As we have shown in the previous numerical calculations, the linewidths of the investigated plasmonic resonances are actually broader than the emission spectrum of the gain medium. In this case, the lasing frequency is determined by the hybridization between the cavity resonance and the emitter. Below, we develop a simple and qualitative coupled mode theory to describe this hybridization process.

We consider two resonant modes, P and Q, corresponding to the amplitudes of the plasmonic cavity mode and the InGaN resonance, respectively. The equations of motion for P and Q are given by

$$\frac{d}{dt}P = [-i\omega_P - \gamma_P]P + igQ, \qquad (S5)$$

$$\frac{d}{dt}Q = [-i\omega_Q - \gamma_Q]Q + igP. \qquad (S6)$$

To normalize the amplitudes, we define $|P|^2$ and $|Q|^2$ to be the numbers of photons inside the corresponding modes. Each resonance is characterized by two parameters: the resonant frequency, $\omega_{P(Q)}$, and the damping rate, $\gamma_{P(Q)}$. g is the coupling coefficient between the two modes, and g^2 is directly related to the modal gain coefficient of the hybridized mode. To see this, we substitute Eq. (S6) into Eq. (S5) after Fourier transformation:

$$-i\omega P = (-i\omega_P - \gamma_P)P + \frac{g^2(-i\omega + i\omega_Q - \gamma_Q)}{(\omega - \omega_Q)^2 + \gamma_Q^2}P. \qquad (S7)$$

The imaginary part of the last term in Eq. (S7) is associated with the frequency shift resulting from the hybridization, while the real part represents an additional gain or loss, with $g^2 > 0$ corresponding to a lossy medium (not relevant to the present experiment) and $g^2 < 0$ a gain medium (corresponding to the present experiment).

On the other hand, we consider the physical situation of a gain medium embedded in a plasmonic cavity. The permittivity of the gain medium is given by Eq. (S4). When $\omega = \omega_G$, the rate of modal gain is given by $W = \frac{\omega_p^2}{4\lambda_G}\int_G d^3x\,|E|^2$, where the integration is over the gain medium. After normalizing with the modal energy, we can compare the rate of gain with that from Eq. (S7) and equate $\frac{W}{U} = -2g^2/\gamma_Q$. With the mode volume defined in Eq. (S3), g can be related to the carrier density and mode volume according to

$$g^2 = -\frac{1}{4}\frac{\omega_p^2 V_{rod}}{\varepsilon_\infty^g V_{mode}}. \qquad (S8)$$

Equations (S5) and (S6) can be solved for their eigenfrequencies, which are given by

$$\omega = \frac{1}{2}(\omega_P * + \omega_Q * \pm \sqrt{4g^2 + (\omega_P * - \omega_Q *)^2}), \qquad (S9)$$

where we have defined $\omega_P* = \omega_P - i\gamma_P$ and $\omega_Q* = \omega_Q - i\gamma_Q$. The spectral evolution of the two complex-valued roots $\omega \equiv \omega_r + i\omega_i$ of Eq. (S9), one of which is close to ω_P and the other to ω_Q, as functions of the coupling coefficient g^2, is shown in Fig. S3A. As the gain coefficient increases and g^2 becomes more negative, the resonant frequencies of the two modes are pulled toward each other. In addition, the linewidth of the resonant mode that has a higher Q-factor narrows down to zero and leads to lasing as its complex-valued eigenfrequency approaches the real axis in the complex (ω_r, ω_i) plane. The resonant frequencies and the damping rates of the resonant modes are calculated from the previous eigenmode simulations according to $\omega_{P(Q)} = 2\pi c/\lambda_{P(Q)}$ and $\gamma_{P(Q)} = \omega_{P(Q)}/2Q_{P(Q)}$, where $\lambda_{P(Q)}$ is the resonant wavelength and $Q_{P(Q)}$ is the quality factor. In Fig. S3B, we show the linewidth narrowing of the dipolar ($n = 5$) and quadrupolar ($n = 4$) resonances with (ω_P, ω_Q, γ_P, γ_Q) taken from the FEM calculations.

Figure S3C shows the experimentally observed effect of frequency pulling with increasing pumping power, which is in accordance with the coupled mode picture. The blue shifting is caused by pulling of the photoluminescence mode toward the plasmonic resonances, since the Q-factor of the emission band is higher than both plasmonic modes.

In Fig. S3D, we compare the threshold value of g with various Q-factors and also different frequency detunings of the plasmonic modes. The emission is centered at $\lambda = 510$ nm with a bandwidth of 30 nm. As the plot shows, both higher Q-factor for the mode and frequency matching are beneficial in reducing the lasing threshold.

Effects of Scattering from a Granular Surface

The atomically smooth silver surface is critical for reaching the low lasing threshold. Since the cavity mode is strongly confined near the metal surface, scattering from grain boundaries and roughness at the surface of polycrystalline silver tends to induce leakage from the cavity. To investigate the role of an atomically smooth surface and its importance in reducing the lasing threshold we numerically studied the effects of grain boundary and surface roughness, and we compared the resonant mode of a uniform surface to that of a granular surface.

As film thickness increases, a granular silver surface evolves from isolated individual islands to interconnected domains with void space between them (33). To simulate the granular silver, the metal surface was randomly divided into small grains with a characteristic length of 20 nm. We introduce domain walls with $\varepsilon = 1$ to separate different domains. The surface filling ratio was kept at 90%, which is appropriate for the 28-nm-thick film considered here (33). A roughened surface with a 300 nm radius centered at the nanorod was simulated. To reduce computational demand, we assumed inversion symmetries along both in-plane directions (x and y), and simulated only one quadrant of the system. Figure S4 compares the resonant mode for an atomically smooth Ag surface to that for a granular Ag surface. The irregular domain walls of the granular film are detrimental to the confinement of the SPP because they create excessive scattering from the plasmonic cavity, as is indicated by the Poynting vectors shown in Figs. S4A and B. In the case of a granular surface, the mode volume of the dipolar resonance is calculated to be $V_{mode} = 1.77 \times 10^{-20}$ m^3, which is about four times the mode volume for a smooth surface. Such poor confinement leads to a much higher lasing threshold.

We also studied the effect of surface roughness, by introducing surface deformation to our model. The deformed surface is shown in Fig. S4E, and is characterized by a peak-to-valley distance of 10 nm and a correlation length of 20 nm (34). The effect of the rough surface is to induce scattering from the cavity, as is indicated by the Poynting flux shown in Fig. S4D. The mode volume of the cavity is calculated to be $V_{mode} = 1.13 \times 10^{-20}$ m^3, which is about three times the mode volume for a smooth surface.
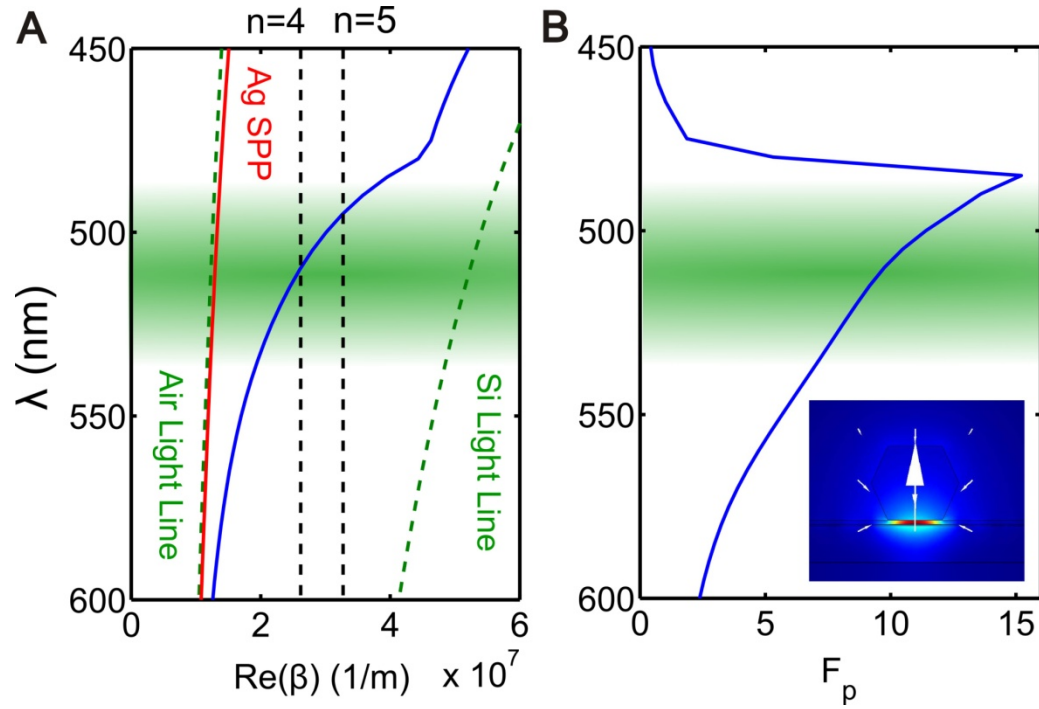
Fig. S1.

(**A**) Dispersion of the confined hybrid SPP between the GaN nanorod and the Ag surface (blue solid line). For comparison, the dispersion of the weakly-confined SPP (no GaN nanorod) is also shown (red solid line). The vertical dashed lines correspond to Fabry-Perot resonant condition $\beta^{(n)} = n\pi / L$. The green area is the emission band of the gain medium. (**B**) The two-dimensional Purcell factor F_P associated with the confined SPP. The inset shows the field distribution of the SPP, with the color map representing $|E|$, and the arrows representing the in-plane E-field.
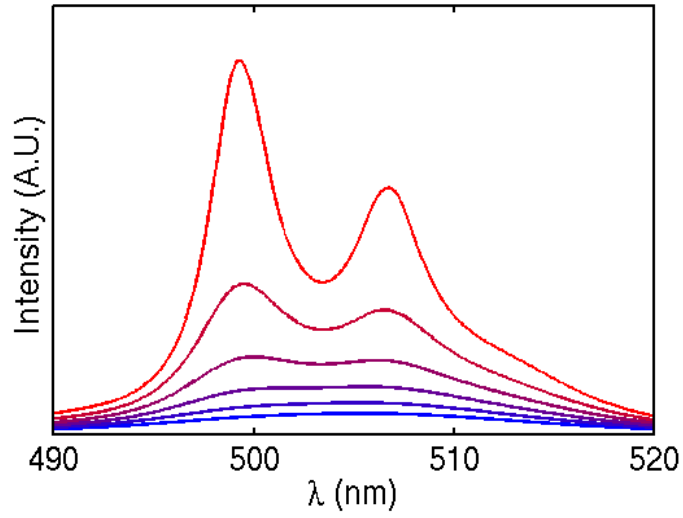
Fig. S2.

Emission spectra of the plasmonic cavity as the carrier density is changed from $n_c = 1.8 \times 10^{19}/\text{cm}^3$ (blue) to $n_c = 4 \times 10^{19}/\text{cm}^3$ (red). Dramatic line narrowing is caused by the gain in the InGaN region of the nanorod.
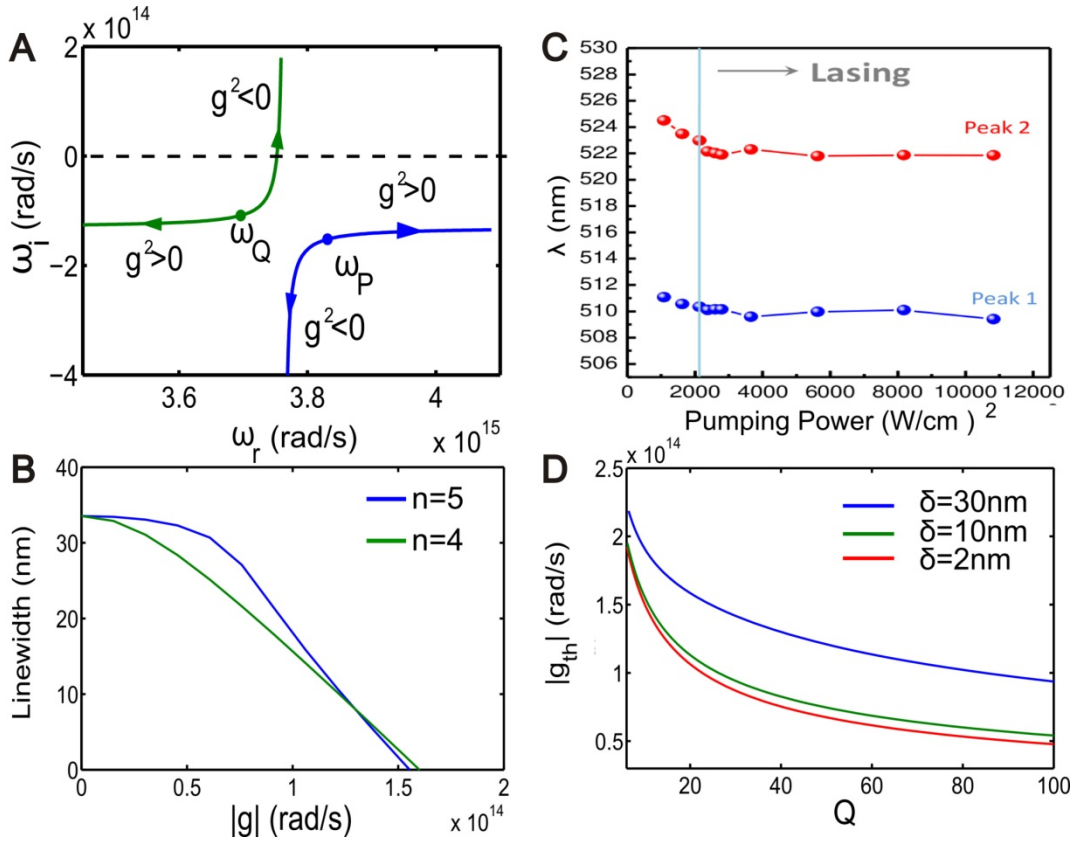
Fig. S3.

Semi-classical model of lasing in the optically pumped SPASER: (**A**) Complex eigenfrequencies $\omega \equiv \omega_r + i\omega_i$ of the hybridized resonances as a function of the coupling gain parameter g^2 defined in the text. Imaginary parts ω_i of the eigenfrequencies correspond to the linewidth of the modes. Lasing occurs when the complex eigenfrequency approaches the real axis in the complex (ω_r, ω_i) plane. The green and blue curves correspond to the two complex-valued solutions of Eq. (S9) for the $n = 5$ (dipole) mode. (**B**) Linewidth narrowing for the two modes with increasing $|g|$. (**C**) Experimentally observed frequency pulling with increasing pumping power. (**D**) Dependence of the lasing threshold on the Q-factor of the plasmonic mode and the detuning from the emission line. δ is the wavelength detuning between the frequency of the hybrid (nanorod/Ag) plasmonic mode and the spectral peak of the photoluminescence. This plot indicates that two factors are important in achieving low-threshold lasing: (i) spectral matching between the hybrid plasmonic mode and the spontaneous emission peak, and (ii) high quality factor of the hybrid plasmonic mode.
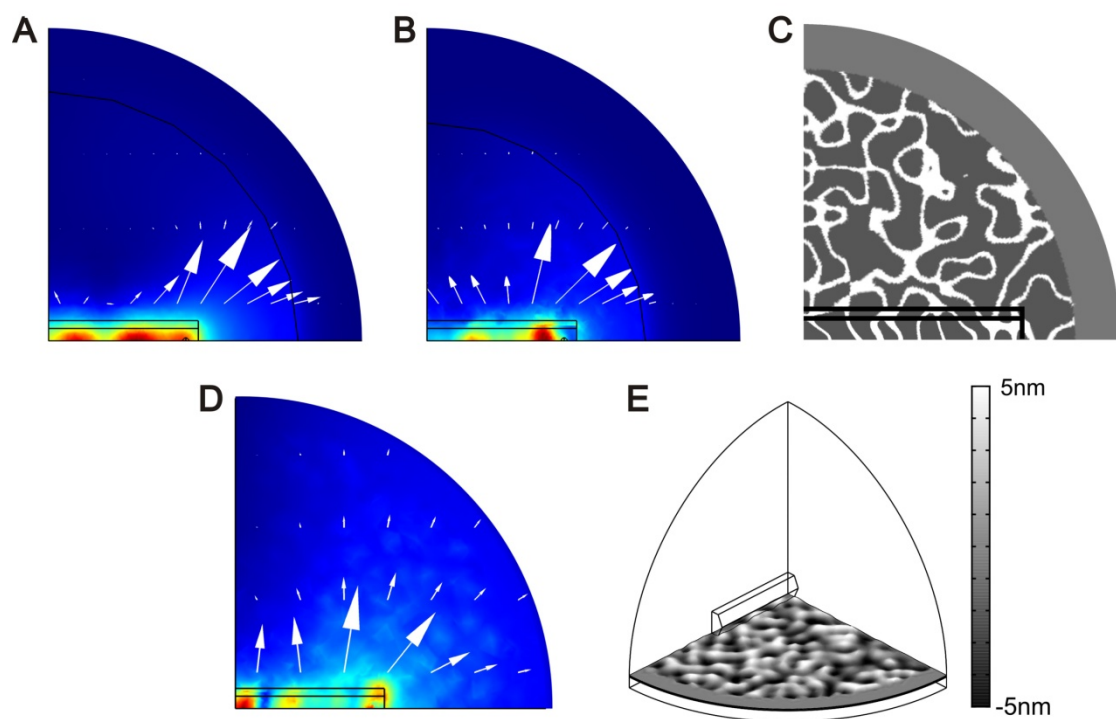
Fig. S4.

Plasmonic resonances, with the nanorod placed on top of (**A**) an atomically smooth Ag film, (**B**) a granular Ag surface with domain walls, and (**D**) a roughened Ag surface with non-uniform thickness. The color maps show the electric field, $|E|$, 10 nm above the surface, and the arrows indicate the Poynting flux. (**C**) Map of the Ag permittivity used to represent the granular surface in (B). White area represents the grain boundaries with $\varepsilon = 1$. (**E**) Illustration of the surface deformation simulated in (D).
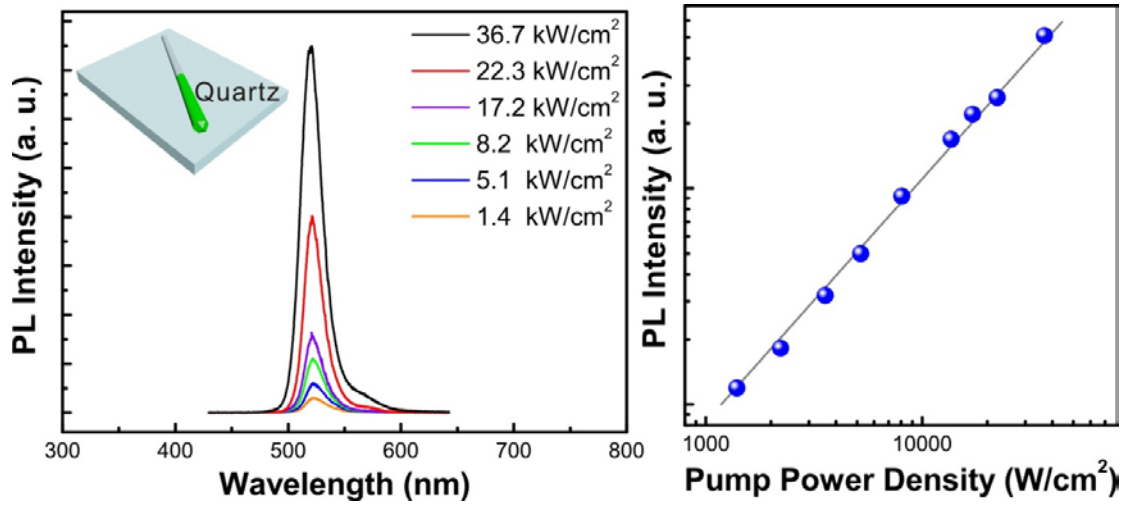
Fig. S5.

Photoluminescence spectra (left) of a single InGaN@GaN core-shell nanorod placed on a quartz substrate at 8 K. The corresponding *L-L* curve (right) shows an intensity vs. power slope very close to one, which confirms that no lasing mode can be observed without the use of an epitaxial Ag plasmonic cavity.
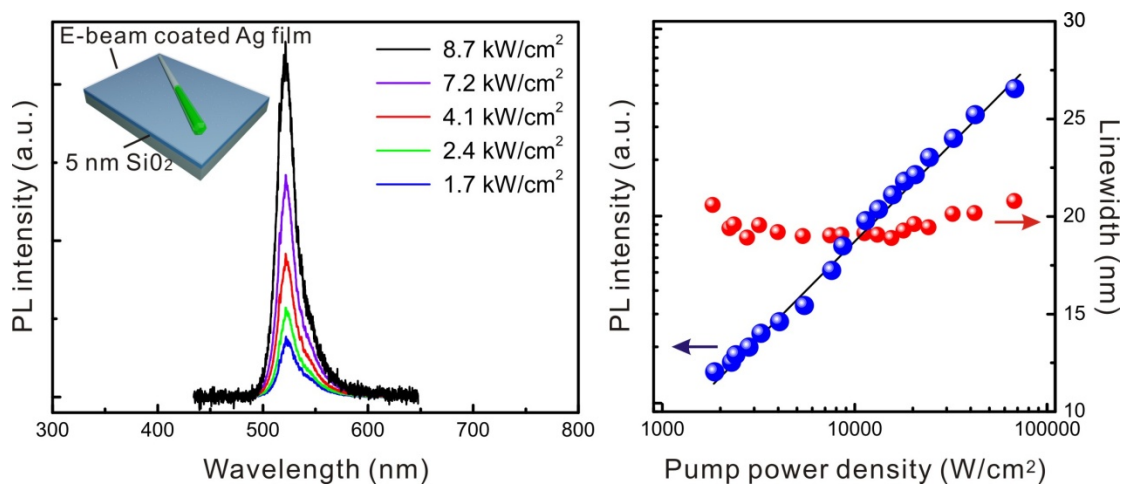
Fig. S6.

Photoluminescence spectra of a single InGaN@ GaN core-shell nanorod placed on a 20-nm-thick polycrystalline Ag film deposited on a quartz substrate. There is a 5-nm-thick SiO_2 gap layer between the nanorod and the Ag film. The measurement was performed at 8 K under CW pumping at 405 nm. Both the polycrystalline Ag film and SiO_2 gap layer were deposited using a UHV electron-beam evaporator. The *L-L* curve and linewidth analysis show that lasing characteristics cannot be observed for the case of the polycrystalline Ag plasmonic cavity.
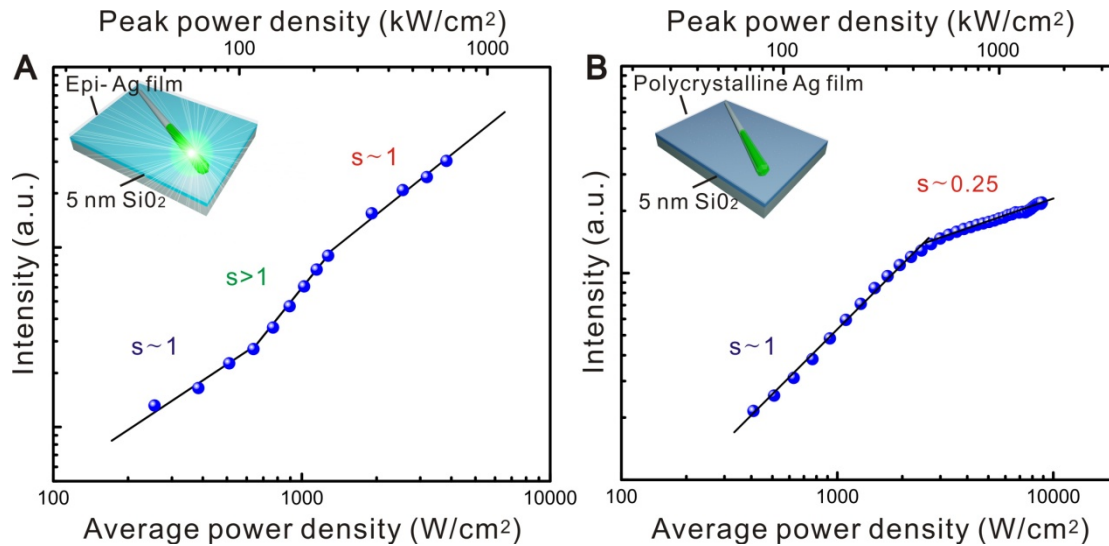
Fig. S7.

Side-by-side comparison of *L-L* curves under pulsed pumping conditions for single nanorods placed on two types of Ag films (epitaxial Ag-on-Si film vs. polycrystalline Ag-on-quartz film). We obtained these curves at 8 K using a pulsed semiconductor diode laser (PicoQuant) with the following characteristics: 405 nm emission wavelength, 70 ps pulse width, and 80 MHz repetition rate. (**A**) The "S"-shaped lasing curve can be clearly observed for the case of epitaxial Ag film. (**B**) The *L-L* curve for a single InGaN@GaN core-shell nanorod deposited on polycrystalline Ag film. Under these pumping conditions, we cannot observe lasing on polycrystalline film for pumping power densities up to 9 kW/cm^2 (i.e., peak pumping power density 1.6 MW/cm^2). The onset of slope (s) less than one (~0.25) at peak power densities greater than 450 kW/cm^2 indicates that local, transient heating effects start to play a significant role in output intensity.

References and Notes

1. S. Noda, Applied physics. Seeking the ultimate nanolaser. *Science* **314**, 260 (2006). doi:10.1126/science.1131322 Medline

2. H. Altug, D. Englund, J. Vučković, Ultrafast photonic crystal nanocavity laser. *Nat. Phys.* **2**, 484 (2006). doi:10.1038/nphys343

3. M. T. Hill, Status and prospects for metallic and plasmonic nano-lasers [Invited]. *J. Opt. Soc. Am. B* **27**, B36 (2010). doi:10.1364/JOSAB.27.000B36

4. K. J. Vahala, Optical microcavities. *Nature* **424**, 839 (2003). doi:10.1038/nature01939 Medline

5. O. Painter *et al.*, Two-dimensional photonic band-gap defect mode laser. *Science* **284**, 1819 (1999). doi:10.1126/science.284.5421.1819 Medline

6. A. Tandaechanurat *et al.*, Lasing oscillation in a three-dimensional photonic crystal nanocavity with a complete bandgap. *Nat. Photonics* **5**, 91 (2011). doi:10.1038/nphoton.2010.286

7. S. Strauf, F. Jahnke, Single quantum dot nanolaser. *Laser Photon. Rev.* **5**, 607 (2011).

8. W. L. Barnes, A. Dereux, T. W. Ebbesen, Surface plasmon subwavelength optics. *Nature* **424**, 824 (2003). doi:10.1038/nature01937 Medline

9. S. A. Maier, H. A. Atwater, Plasmonics: Localization and guiding of electromagnetic energy in metal/dielectric structures. *J. Appl. Phys.* **98**, 011101 (2005). [doi:10.1063/1.1951057](doi:10.1063/1.1951057)

10. D. K. Gramotnev, S. I. Bozhevolnyi, Plasmonics beyond the diffraction limit. *Nat. Photonics* **4**, 83 (2010). doi:10.1038/nphoton.2009.282

11. J. A. Schuller *et al.*, Plasmonics for extreme light concentration and manipulation. *Nat. Mater.* **9**, 193 (2010). doi:10.1038/nmat2630 Medline

12. M. T. Hill *et al.*, Lasing in metallic-coated nanocavities. *Nat. Photonics* **1**, 589 (2007). doi:10.1038/nphoton.2007.171

13. M. P. Nezhad *et al.*, Room-temperature subwavelength metallo-dielectric lasers. *Nat. Photonics* **4**, 395 (2010). doi:10.1038/nphoton.2010.88

14. D. J. Bergman, M. I. Stockman, Surface plasmon amplification by stimulated emission of radiation: Quantum generation of coherent surface plasmons in nanosystems. *Phys. Rev. Lett.* **90**, 027402 (2003). doi:10.1103/PhysRevLett.90.027402 Medline

15. M. I. Stockman, The spaser as a nanoscale quantum generator and ultrafast amplifier. *J. Opt.* **12**, 024004 (2010). [doi:10.1088/2040-8978/12/2/024004](doi:10.1088/2040-8978/12/2/024004)

16. M. A. Noginov *et al.*, Demonstration of a spaser-based nanolaser. *Nature* **460**, 1110 (2009). doi:10.1038/nature08318 Medline

17. R. F. Oulton *et al.*, Plasmon lasers at deep subwavelength scale. *Nature* **461**, 629 (2009). doi:10.1038/nature08364 Medline

18. R.-M. Ma, R. F. Oulton, V. J. Sorger, G. Bartal, X. Zhang, Room-temperature sub-diffraction-limited plasmon laser by total internal reflection. *Nat. Mater.* **10**, 110 (2011). doi:10.1038/nmat2919 Medline

19. C.-Y. Wu *et al.*, Plasmonic green nanolaser based on a metal-oxide-semiconductor structure. *Nano Lett.* **11**, 4256 (2011). doi:10.1021/nl2022477 Medline

20. P. R. West *et al.*, Searching for better plasmonic materials. *Laser Photon. Rev.* **4**, 795 (2010). doi:10.1002/lpor.200900055

21. P. Nagpal, N. C. Lindquist, S.-H. Oh, D. J. Norris, Ultrasmooth patterned metals for plasmonics and metamaterials. *Science* **325**, 594 (2009). doi:10.1126/science.1174655 Medline

22. J.-S. Huang *et al.*, Atomically flat single-crystalline gold nanostructures for plasmonic nanocircuitry. *Nat. Commun.* **1**, 150 (2010). doi:10.1038/ncomms1143 Medline

23. K. L. Shaklee, R. E. Nahory, R. F. Leheny, Optical gain in semiconductors. *J. Lumin.* **7**, 284 (1973). doi:10.1016/0022-2313(73)90072-0

24. A. R. Smith, K.-J. Chao, Q. Niu, C. K. Shih, Formation of atomically flat silver films on GaAs with a "silver mean" quasi periodicity. *Science* **273**, 226 (1996). doi:10.1126/science.273.5272.226 Medline

25. H. Yu *et al.*, Quantitative determination of the metastability of flat Ag overlayers on GaAs(110). *Phys. Rev. Lett.* **88**, 016102 (2001). doi:10.1103/PhysRevLett.88.016102 Medline

26. Information on methods, analyses, and simulations can be found in the supplementary materials available on *Science* Online.

27. R. F. Oulton, V. J. Sorger, D. A. Genov, D. F. P. Pile, X. Zhang, A hybrid plasmonic waveguide for subwavelength confinement and long-range propagation. *Nat. Photonics* **2**, 496 (2008). doi:10.1038/nphoton.2008.131

28. Y.-J. Lu, H.-W. Lin, H.-Y. Chen, Y.-C. Yang, S. Gwo, Single InGaN nanodisk light emitting diodes as full-color subwavelength light sources. *Appl. Phys. Lett.* **98**, 233101 (2011). doi:10.1063/1.3597211

29. J. D. Jackson, *Classical Electrodynamics* (Wiley, New York, ed. 3, 1999), ch. 9.

30. H.-Y. Chen, H.-W. Lin, C.-H. Shen, S. Gwo, Structure and photoluminescence properties of epitaxially oriented GaN nanorods grown on Si(111) by plasma-assisted molecular-beam epitaxy. *Appl. Phys. Lett.* **89**, 243105 (2006). doi:10.1063/1.2404597DOI: 10.1063/1.2404597

31. J. Müller *et al.*, Gain analysis of blue nitride-based lasers by small signal modulation. *Appl. Phys. Lett.* **96**, 131105 (2010). doi:10.1063/1.3372637DOI: 10.1063/1.3372637

32. Yu. A. Vlasov, K. Luterova, I. Pelant, B. Hönerlage, V. N. Astratov, Optical gain of CdS quantum dots embedded in 3D photonic crystals. *Thin Solid Films* **318**, 93 (1998). doi:10.1016/S0040-6090(97)01146-2DOI: 10.1016/S0040-6090(97)01146-2

33. H. Wei, H. Eilers, From silver nanoparticles to thin films: Evolution of microstructure and electrical conduction on glass substrates. *J. Phys. Chem. Solids* **70**, 459 (2009). [doi:10.1016/j.jpcs.2008.11.012DOI: 10.1016/j.jpcs.2008.11.012](#)

34. V. J. Logeeswaran *et al*., Ultrasmooth silver thin films deposited with a germanium nucleation layer. *Nano Lett.* **9**, 178 (2009). [doi:10.1021/nl8027476DOI: 10.1021/nl8027476](#) [Medline](#)

Going Green with Nanophotonics

Plasmons are optically induced collective electronic excitations tightly confined to the surface of a metal, with silver being the metal of choice. The subwavelength confinement offers the opportunity to shrink optoelectronic circuits to the nanometer scale. However, scattering processes within the metal lead to losses. Lu et al. (p. 450) developed a process to produce atomically smooth layers of silver, epitaxially grown on silicon substrates. A cavity in the silver layer is capped with a SiO insulating layer and an AlGaN nanorod was used to produce a low-threshold emission at green wavelengths.